Experimental demonstration of a nanolaser with a sub-μA threshold current

Dimopoulos, Evangelos; Xiong, Meng; Sakanas, Aurimas; Marchevsky, Andrey; Dong, Gaoneng; Yu, Yi; Semenova, Elizaveta; Mørk, Jesper; Yvind, Kresten

Published in:
Optica

Link to article, DOI:
10.1364/OPTICA.488604

Publication date:
2023

Document Version
Publisher's PDF, also known as Version of record

OPTICA

Experimental demonstration of a nanolaser with a sub-μA threshold current

Evangelos Dimopoulos,[1,2] Meng Xiong,[1,2] Aurimas Sakanas,[1] Andrey Marchevsky,[1] Gaoneng Dong,[1,2] Yi Yu,[1,2] Elizaveta Semenova,[1,2] Jesper Mørk,[1,2] and Kresten Yvind[1,2,*]

[1]Department of Electrical and Photonics Engineering, Technical University of Denmark, 2800 Kgs. Lyngby, Denmark
[2]NanoPhoton—Center for Nanophotonics, Technical University of Denmark, 2800 Kgs. Lyngby, Denmark
*kryv@dtu.dk

Received 23 February 2023; revised 15 June 2023; accepted 26 June 2023; published 24 July 2023

We demonstrate a nano-buried-heterostructure photonic crystal laser exhibiting an ultralow threshold of 730 nA at telecom wavelengths. This breakthrough was achieved by reducing the doping-induced losses of the laser cavity, enabling the efficient miniaturization of the active region. The laser can be directly modulated at 3 GHz at an energy cost of 1 fJ/bit, and a comparison to longer lasers is given. To the best of our knowledge, this is the lowest threshold reported for any laser operating at room temperature, facilitating on-chip links with ultralow energy consumption.

https://doi.org/10.1364/OPTICA.488604

Semiconductor lasers with high efficiency and ultralow operating energy are required for on-chip optical interconnects to replace the currently used electrical wiring that is limited by excessive power consumption and heat dissipation [1]. Diode lasers exhibit efficient high-speed operation when operated close to the laser threshold. Therefore, realizing ultracompact lasers with a low threshold current and low drive voltage is an important goal. High refractive index contrast structures like photonic crystals (PhCs) are considered the most promising candidates for on-chip applications since PhC cavities provide high quality factors (Q factors) and wavelength-scale mode volumes, enabling the required miniaturization of the active material and allowing electrical injection in a planar geometry.

In the last decades, significant research on PhC lasers has been conducted, and optically pumped long-wavelength PhC lasers with cw wave room temperature operation have been demonstrated [2–6], achieving an ultralow calculated absorbed power at a threshold of 210 nW [7]. However, electrical pumping has proven inherently challenging, and only recently electrically driven PhC lasers with cw room temperature operation have been realized [8–10]. Furthermore, introducing metals and dopants limits the Q factor of the laser cavity; thus, the lowest attainable threshold for electrically driven PhC lasers on the InP and InP-on-Si platforms has converged to around 5 μA [11,12] and 10 μA [13,14], respectively. Nevertheless, numerical calculations using reasonable laser parameter values [15] show that the currently achieved thresholds are still an order of magnitude higher than what is theoretically possible.

In this work, we demonstrated a cw PhC laser with an ultralow threshold of 730 nA emitting at telecom wavelengths. To the best of our knowledge, this is the lowest reported threshold current for any laser at room temperature. Additionally, we achieved operating voltages below 1 V and direct modulation at 3 GHz with an energy cost of 1 fJ/bit. This breakthrough was achieved by a laser design that overcomes the low Q factor limitation imposed by the doping-induced losses [14], allowing the efficient downscaling of the buried-heterostructure (BH) active region.

A schematic diagram of the nano-BH laser is shown in Fig. 1(a). The laser is based on a 250 nm thick InP PhC membrane heterogeneously bonded on an SiO_2/Si platform via direct bonding [16]. A PhC cavity with seven missing air holes (L7 cavity) is used to confine the optical field [17], and an ultrasmall BH active region is used to confine the carriers vertically and laterally. The PhC lattice

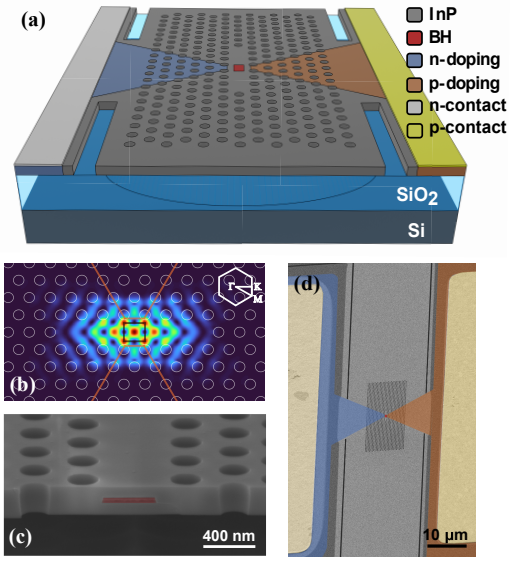

Fig. 1. (a) Schematic diagram of the nano-BH L7 laser. (b) Simulated electric field profile. The PhC holes and the active and doping regions are outlined in white, black, and orange, respectively. (c) Colored cross-sectional SEM image of the BH. (d) Colored bird's-eye view SEM image of the device.

constant and hole radius were chosen as 440 nm and 120 nm, respectively, to achieve resonance at telecom wavelengths. The electric field profile of the lasing mode is shown in Fig. 1(b). The volume of the nano-BH region is $440 \times 400 \times 8\ \text{nm}^3$, comprised of a single InGaAsP/InAlGaAs-based quantum well (QW), whose emission is centered around 1550 nm. Figure 1(c) illustrates the cross-sectional view of a PhC line defect featuring the BH region highlighted in red. A lateral carrier injection scheme is used to inject carriers in the BH region. The n-doped and p-doped regions have been formed via Si ion implantation and Zn thermal diffusion, respectively. Details on the fabrication method can be found in [14]. A bird's-eye view SEM image of the device is depicted in Fig. 1(d).

Reducing the size of the active material is generally beneficial for low power consumption; however, a high Q factor is critical due to the corresponding decrease in the modal gain. In previous work, we showed that the optical absorption of the p-doping region is the main loss channel that ultimately determines the Q factor of the laser cavity, and the absorption coefficient of the p-doped region was experimentally determined to be $120\ \text{cm}^{-1}$ [14]. Since the doping profile normally matches the BH length, we opted for a longer optical cavity to reduce the mode's overlap with the doping region, while maintaining a sufficiently high confinement factor Γ of 0.5%.

In Fig. 2(a), the collected optical power and the applied voltage versus the injection current are shown. Part of the laser light that leaks vertically is collected via a 50× long working distance objective coupled to a multimode fiber and is then measured using an optical spectrum analyzer (OSA). The inset of Fig. 2(a) shows a microscope image of the laser captured by an IR camera. The laser threshold current is 730 nA and was extracted from the double-log plot of the L-I curve shown in Fig. 2(b). Due to a high β factor, the threshold was calculated numerically as the maximum of the derivative of the $\log(L)$-$\log(I)$ curve [18]. The applied voltage at the threshold is 0.83 V; thus, the threshold electrical input power is 610 nW ($P_{in} = IV$).

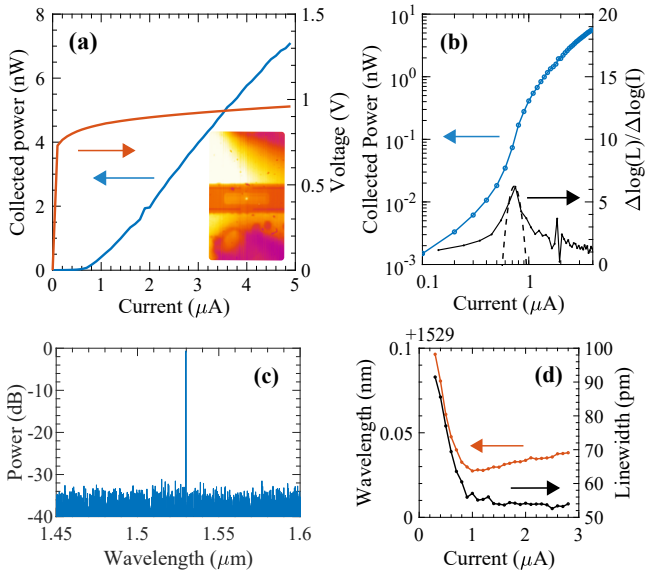

Fig. 2. (a) Collected output power and applied voltage as a function of injected current. Inset: microscope picture of the laser. (b) Log–log plot of the LI curve and its derivative. (c) Laser spectrum at 5 μA. (d) Laser wavelength and linewidth as a function of injected current.

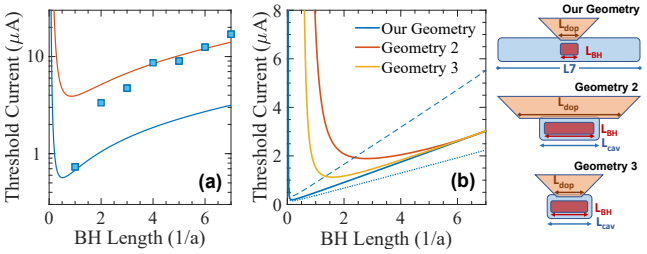

Fig. 3. (a) Threshold current versus the BH length of L7 lasers. The solid lines represent theoretical fits. (b) Laser threshold for three geometries: Our Geometry, where the doping length follows the BH length in a fixed L7 cavity; Geometry 2, where the cavity length follows the BH, while the doping length is fixed at $7a$; and Geometry 3, where all three components are varied simultaneously. The blue dashed and dotted lines illustrate the threshold in our geometry for different doping-induced losses.

The laser emits at 1529 nm and achieves single-mode operation, as shown in the emission spectrum displayed in Fig. 2(c). The evolution of the laser wavelength and the linewidth close to the threshold is shown in Fig. 2(d). In the spontaneous emission regime, the resonance blueshifts due to the band-filling effect. Above the threshold, the carrier density is clamped, and the lasing wavelength redshifts due to thermal effects. The linewidth exhibits a kink near the threshold as its value saturates at the resolution limit of the OSA. By tracking the laser wavelength using controlled variations to the device temperature, we deduced that the laser exhibits a very modest self-heating, estimated to be below 3 K at $10 \cdot I_{\text{th}}$.

The laser threshold of L7 lasers with varying BH lengths is shown in Fig. 3(a), exhibiting a strong reduction of the threshold current for shorter active regions. Assuming a logarithmic gain model, as appropriate for a QW structure [15], the threshold current can be expressed as

$$I_{\text{th}} = \frac{J_0 L_{\text{BH}}}{\eta_i} \exp\left(\frac{a_{\text{mir}} + \Gamma_{\text{dop}} a_{\text{dop}}}{\Gamma_{\text{act}} g_0}\right). \quad (1)$$

Here, L_{BH} is the length of the nano-BH, J_0 is a characteristic current density, η_i is the injection efficiency, $\Gamma_{\text{act}} g_0$ is the modal gain, and α_{dop} and α_{mir} are the doping losses and mirror losses, respectively. The gain coefficient is represented as g_0, while $\Gamma_{\text{act,dop}}$ are the modal confinement factors for the active material and the doping, respectively. The modal gain and the doping-induced modal losses depend on the respective BH and doping lengths, while the mirror losses depend only on the cavity length. Theoretically, a characteristic BH length should exist below which the total losses dominate, and the reduction of the modal gain leads to an increased threshold. However, such a characteristic length has not been observed in our experiments, suggesting that further miniaturization is possible.

We believe, to the best of our knowledge, that this is the first demonstration of sub-μA lasing and it is attributed to the efficient miniaturization of the active material. Unlike previous realizations [12,14], we decoupled the BH and doping length L_{dop} from the cavity length L_{cav}. This strategy is possible because the modal gain and the doping-induced modal absorption scale similarly with the BH length, as shown in Fig. S3(a); thus, the characteristic length minimizing the threshold will only depend on the mirror losses, which are inversely proportional to the cavity length. Figure 3(b) depicts the laser threshold dependence on the BH length for three distinct geometries: our configuration, where L_{BH} and L_{dop} are

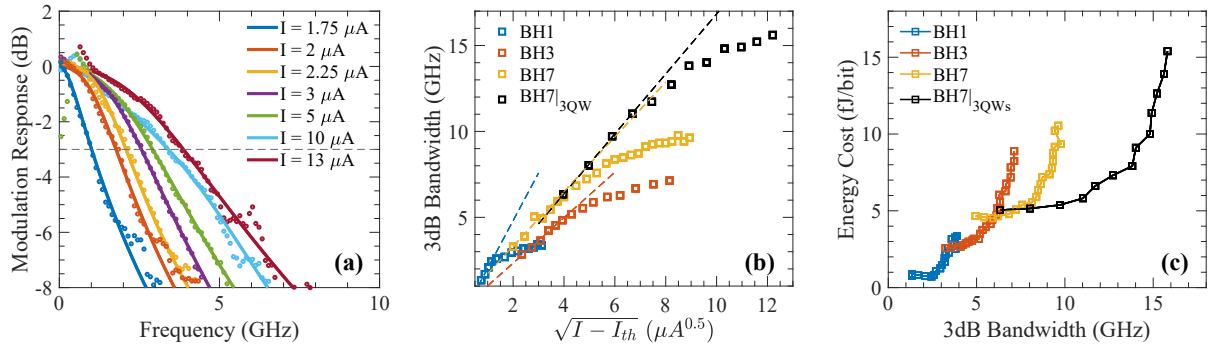

Fig. 4. (a) Small-signal response of the laser. (b) Modulation bandwidth versus the square root of the applied current minus the threshold current for different active material sizes. (c) Comparison of the energy cost per bit as a function of the modulation bandwidth for different lasers.

varied in a fixed L7 cavity; a case where L_{BH} and L_{cav} are varied while the doping length is fixed at $7a$; and the case where all three components are varied simultaneously. A sketch of these geometries is shown at the outset of Fig. 3(b). Comparing the threshold values for these different configurations, it became apparent that the lowest threshold is achieved by selecting a high-Q cavity with an extended length, while simultaneously varying the BH and doping lengths. This approach compensates for the reduction in modal gain associated with a shorter BH length by mitigating the doping-induced losses. Details on the laser modeling and the parameters used for the threshold analysis are given in Sections 2 and 3 of Supplement 1.

Additionally, the blue dashed and dotted lines in Fig. 3(b) illustrate the threshold of our geometry when the doping-induced modal losses are either doubled or halved, respectively, compared to the blue solid line. The reduction of doping-induced losses can be accomplished by increasing the doping offset or by decreasing the p-doping level. However, employing the former method is anticipated to lead to a decrease in the injection efficiency, whereas implementing the latter method is expected to increase the resistance, thereby necessitating higher applied voltage that may impact the wall-plug efficiency.

The solid lines of Fig. 3(a) show solutions to Eq. (1), where J_0 is 150 nA/440 nm, and η_i is 35% and 9% for the blue and orange line, respectively. However, we are not able to fit all the experimental data using one set of parameters. We attribute this to two issues. First, the experimental threshold current shown for a given L_{BH} is the minimum value obtained from a batch of nominally identical devices. The threshold statistics are included in Section 5 of Supplement 1. However, fabrication-induced variations are significant since we are working at the limit of our fabrication techniques. Second, the theory we use was developed for macroscopic lasers and assumes average propagation losses unaffected by the possible variation of the slow light effect and constant electrical injection efficiency. As a result, an improved analysis and further characterization of nanolasers are needed to unveil the laser physics on the microscale and nanoscale.

We also investigated the dynamic properties of our nanolasers. The small-signal direct modulation response (S_{21}) of the laser was measured using a vector network analyzer. Figure 4(a) shows the small-signal response of the laser for different injected powers. The response function exhibits characteristic bandwidth increases at higher injected currents, and its 3 dB bandwidth was extracted from the fitted response function given by [15]

$$H(f) = A\,\frac{f_r^2}{f_r^2 - f^2 + j\frac{f}{2\pi}\gamma}\,\frac{1}{1 + j\frac{f}{f_p}}, \tag{2}$$

where f_r is the resonant oscillation frequency of the laser, γ is the damping factor, f_p is the parasitic cut-off frequency, and A is a scaling factor. The parasitic frequency is related to the RC time constant ($f_p = 1/2\pi RC$), where R is the resistance of the device and C is the parasitic capacitance. In this calculation, a RC constant is chosen as 5–12 ps, depending on the device. Due to the small cavity size and the high cavity Q factor, the response is overdamped. Furthermore, the D-factor and the K-factor are calculated as 44.8 GHz/mA$^{0.5}$ and 1.5 ns, respectively, while the modulation efficiency is 68.6 GHz/mA$^{0.5}$. The modulation efficiency of the laser is multiple times higher than this of high-speed vertical cavity surface emitting lasers (VCSELs) [19]; however, the modulation frequency saturates above 3 GHz due to the high damping.

For comparison, Fig. 4(b) depicts the 3 dB bandwidth versus the square root of the injected current minus the threshold current for different L7 cavity lasers with varying active material sizes. Each laser is identified by the length of its active region in units of the PhC lattice constant. In addition to the single QW designs, a 3QW-BH7 laser is shown for comparison. The modulation bandwidth is proportional to the square root of the current above threshold, and a linear fit is used to extract the modulation efficiency. The values of the modulation efficiency and the D and K factors for the different lasers are summarized in Table 1 and defined in Section 6 of Supplement 1. For the 1QW samples, the D-factor variation scales with the photon volume for the different lasers. The 3QW laser operation requires a lower carrier density, and thus a higher differential gain is expected. However, the D factor is very similar to its 1QW counterparts, suggesting that it should have a lower injection efficiency. On the other hand, the damping increases for smaller BH lasers since the K factor increases with the increasing photon lifetime. Furthermore, the maximum modulation frequency $f_{3\,\mathrm{dB}}^{\mathrm{max}}$ depends strongly on the laser size

Table 1. Small-Signal Modulation Characteristics of L7 Lasers

BH Variant	Mod. Efficiency (GHz mA$^{-1/2}$)	D Factor (GHz mA$^{-1/2}$)	K Factor (ns)
BH1	68.6	44.8	1.49
BH3	48.8	43.4	0.72
BH7	41.5	34.4	0.18
BH7$\|_{3\mathrm{QW}}$	60.2	35.5	0.16

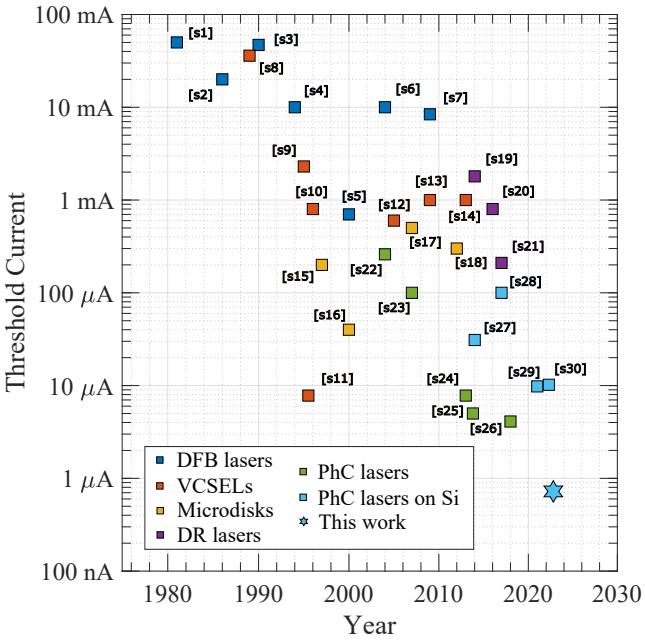

Fig. 5. Historical evolution of the laser threshold in semiconductor lasers. References are included in Supplement 1.

since it is inversely proportional to the K factor; $f_{3\,\mathrm{dB}}^{\max} = 2\pi\sqrt{2}/K$. Note, though, that higher damping can be advantageous for high-quality data transmission [20].

In Fig. 2(c), the energy cost per "1" bit for L7 cavity lasers with varying active material sizes is plotted against the 3 dB bandwidth. The energy cost is estimated as $\mathrm{EC} = P_{in}/1.3 f_{3\,\mathrm{dB}}$ [21], where $f_{3\,\mathrm{dB}}$ is the 3 dB bandwidth of the small-signal response function. The BH1 laser can operate at the typical processor clock rates of 2–3 GHz [1] with less than a 1 fJ/bit energy cost for a "1" bit, which corresponds to an average below 0.5 fJ/bit for NRZ modulation with an equal number of "0" and "1" bits. The longer BH lasers can achieve higher data rates, but at an excessive energy cost; i.e., it is energetically favorable to achieve a given data rate by multiplexing multiple BH1 lasers.

The historical evolution of the threshold for different types of semiconductor lasers is shown in Fig. 5. Following all recent achievements in semiconductor lasers, an exponential decrease in the threshold current can be observed. Distributed feedback lasers (DFBs) were among the first diode lasers to be developed and are massively employed for telecom applications. However, their threshold has saturated to 1 mA due to the weak optical confinement that poses a lower limit to the active material size. Recently, this limit has been lifted by membrane-based lasers with a distributed reflector (DR) that enables efficient lasing with tens of microns long BH active regions that can be used for chip-to-chip computer-com applications. VCSELs have also demonstrated exemplary performance and are the industry's standard for short distance datacom applications. Although reducing the threshold in VCSELs is possible [22], vertical emission is not preferable for on-chip computer-com applications where the coupling losses should be minimal. Similarly, microdisk lasers have achieved low threshold lasing; however, the inherent difficulties on shrinking the mode volume while maintaining high Q factor prohibits further miniaturization. All the above issues can be addressed with in-plane PhC nanolasers, drastically reducing the mode volume while maintaining high intrinsic Q-factors. Good performance has been demonstrated in both III-V and Si substrates.

In summary, we have designed and experimentally demonstrated a photonic crystal nanolaser that exhibits an ultralow threshold current of 730 nA in cw room-temperature operation. The laser comprises a submicron BH active region with a single quantum well and a matching doping profile that causes minimal absorption. Furthermore, small-signal modulation measurements showed that as the active material and absorption losses are reduced, the maximum modulation bandwidth is reduced due to damping. An energy cost of less than 1 fJ per bit is achieved at a modulation frequency of 3 GHz. This laser type is a strong candidate for future on-chip interconnects requiring efficient low-power consumption light sources.

Funding. Villum Fonden (8692, NATEC); European Research Council (834410, FANO); Danmarks Grundforskningsfond (DNRF147, NanoPhoton).

Disclosures. The authors declare no conflicts of interest.

Data availability. Data underlying the results presented in this paper may be obtained from the authors upon reasonable request.

Supplemental document. See Supplement 1 for supporting content.

REFERENCES

1. D. A. B. Miller, J. Lightwave Technol. **35**, 346 (2017).
2. M. Nomura, S. Iwamoto, K. Watanabe, N. Kumagai, Y. Nakata, S. Ishida, and Y. Arakawa, Opt. Express **14**, 6308 (2006).
3. S. Matsuo, A. Shinya, T. Kakitsuka, K. Nozaki, T. Segawa, T. Sato, Y. Kawaguchi, and M. Notomi, Nat. Photonics **4**, 648 (2010).
4. S. Matsuo, A. Shinya, C.-H. Chen, K. Nozaki, T. Sato, Y. Kawaguchi, H. Taniyama, and M. Notomi, Opt. Express **19**, 2242 (2011).
5. W. Xue, Y. Yu, L. Ottaviano, Y. Chen, E. Semenova, K. Yvind, and J. Mork, Phys. Rev. Lett. **116**, 063901 (2016).
6. Y. Yu, A. Sakanas, A. R. Zali, E. Semenova, K. Yvind, and J. Mørk, Nat. Photonics **15**, 758 (2021).
7. H. Jang, I. Karnadi, P. Pramudita, J. H. Song, K. Soo Kim, and Y. H. Lee, Nat. Commun. **6**, 8276 (2015).
8. K. Takeda, T. Sato, A. Shinya, K. Nozaki, W. Kobayashi, H. Taniyama, M. Notomi, K. Hasebe, T. Kakitsuka, and S. Matsuo, Nat. Photonics **7**, 569 (2013).
9. K. Takeda, T. Sato, T. Fujii, E. Kuramochi, M. Notomi, K. Hasebe, T. Kakitsuka, and S. Matsuo, Opt. Express **23**, 702 (2015).
10. G. Crosnier, D. Sanchez, S. Bouchoule, P. Monnier, G. Beaudoin, I. Sagnes, R. Raj, and F. Raineri, Nat. Photonics **11**, 297 (2017).
11. K.-Y. Jeong, Y.-S. No, Y. Hwang, K. S. Kim, M.-K. Seo, H.-G. Park, and Y.-H. Lee, Nat. Commun. **4**, 2822 (2013).
12. E. Kuramochi, H. Duprez, J. Kim, M. Takiguchi, K. Takeda, T. Fujii, K. Nozaki, A. Shinya, H. Sumikura, H. Taniyama, S. Matsuo, and M. Notomi, Opt. Express **26**, 26598 (2018).
13. K. Takeda, T. Tsurugaya, T. Fujii, A. Shinya, Y. Maeda, T. Tsuchizawa, H. Nishi, M. Notomi, T. Kakitsuka, and S. Matsuo, Opt. Express **29**, 26082 (2021).
14. E. Dimopoulos, A. Sakanas, A. Marchevsky, M. Xiong, Y. Yu, E. Semenova, J. Mørk, and K. Yvind, Laser Photon. Rev. **16**, 2200109 (2022).
15. L. A. Coldren and S. Corzine, *Diode Lasers and Photonic Integrated Circuits* (Wiley, 1995).
16. A. Sakanas, E. Semenova, L. Ottaviano, J. Mørk, and K. Yvind, Microelectron. Eng. **214**, 93 (2019).
17. M. Saldutti, M. Xiong, E. Dimopoulos, Y. Yu, M. Gioannini, and J. Mørk, Nanomaterials **11**, 3030 (2021).
18. C. Z. Ning, IEEE J. Sel. Top. Quantum Electron. **19**, 1503604 (2013).
19. S. Spiga, W. Soenen, A. Andrejew, D. M. Schoke, X. Yin, J. Bauwelinck, G. Boehm, and M. C. Amann, J. Lightwave Technol. **35**, 727 (2017).
20. E. P. Haglund, P. Westbergh, J. S. Gustavsson, and A. Larsson, J. Lightwave Technol. **33**, 795 (2015).
21. R. S. Tucker, J. M. Wiesenfeld, P. M. Downey, and J. E. Bowers, Appl. Phys. Lett. **48**, 1707 (1986).
22. G. Yang, M. MacDougal, and P. Dapkus, Electron. Lett. **31**, 886 (1995).